E. coli do not count single molecules

Henry H. Mattingly†[,1], Keita Kamino†[,2], Jude Ong‡[,3], Rafaela Kottou‡[,3], Thierry Emonet*[,3,4,5], Benjamin B. Machta*[,4,5]

[1] Center for Computational Biology, Flatiron Institute
[2] Institute of Molecular Biology, Academia Sinica
[3] Molecular, Cellular, and Developmental Biology, [4] Physics, and [5] QBio Institute, Yale University

† These authors contributed equally.

‡ These authors contributed equally.

* Correspondence to: Benjamin.machta@yale.edu and Thierry.emonet@yale.edu.

Abstract

Organisms must perform sensory-motor behaviors to survive. What bounds or constraints limit behavioral performance? Previously, we found that the gradient-climbing speed of a chemotaxing *Escherichia coli* is near a bound set by the limited information they acquire from their chemical environments (1). Here we ask what limits their sensory accuracy. Past theoretical analyses have shown that the stochasticity of single molecule arrivals sets a fundamental limit on the precision of chemical sensing (2). Although it has been argued that bacteria approach this limit, direct evidence is lacking. Here, using information theory and quantitative experiments, we find that *E. coli*'s chemosensing is *not* limited by the physics of particle counting. First, we derive the physical limit on the behaviorally-relevant information that any sensor can get about a changing chemical concentration, assuming that every molecule arriving at the sensor is recorded. Then, we derive and measure how much information *E. coli*'s signaling pathway encodes during chemotaxis. We find that *E. coli* encode two orders of magnitude less information than an ideal sensor limited only by shot noise in particle arrivals. These results strongly suggest that constraints other than particle arrival noise limit *E. coli*'s sensory fidelity.

Introduction

Organisms must rapidly and accurately sense their environment, and then act on that sensory information to perform motor behaviors. Despite the importance of these processes for organisms' survival, it is unclear what factors limit sensory fidelity and how this fidelity impacts behavioral performance (3). Past works have demonstrated that physics external to an organism often place fundamental limits on sensing accuracy and have argued that biological sensory systems might approach these limits (4,5,2,6–9). Alternatively, it is possible that other, system-specific constraints combined with demands on cellular resources are instead limiting (10–17). Understanding which constituent processes of a behavior limit performance would reveal relevant constraints on evolution and learning of sensory-motor behaviors.

Escherichia coli chemotaxis is an ideal system to study these questions. Bacteria use the chemotaxis system to navigate chemical gradients, which is important for fitness-relevant behaviors such as climbing quickly or localizing at sources (18–21). Furthermore, we understand in detail how *E. coli* sense and act on chemical signals (22–24). *E. coli* alternate between straight-swimming runs and randomly-reorienting

tumbles (25). As they swim, the local concentrations of attractant chemicals change in time. These extracellular ligands bind to the cell's transmembrane receptors, which modify the activity of receptor-associated CheA kinases inside the cell. CheA phosphorylates the diffusible response regulator CheY, which is dephosphorylated by CheZ. When conditions worsen, kinase activity increases, increasing CheYp concentration. CheYp then binds to the motor and increases the propensity to tumble, biasing the cell's runs towards more favorable chemical environments.

We recently demonstrated that *E. coli* chemotaxis is information-limited: cells climb shallow gradients near a bound set by their sensory capabilities (1). First, we showed theoretically that the rate at which a cell encodes information about chemical signals sets an upper limit on its gradient-climbing speed. Then, through a combination of single-cell Förster resonance energy transfer (FRET) experiments and measurements of cells swimming in gradients, we found that a typical *E. coli* cell gets very little information—about 0.01 bits/s in a centimeter-long gradient—but efficiently uses this information to climb gradients at speeds near the theoretical limit. This suggests that a bacterium with a more accurate sensor would climb gradients faster, likely increasing their fitness.

What prevents *E. coli* from obtaining more information during chemotaxis? In their classic work, Berg and Purcell demonstrated that the stochastic arrival of particles at the cell surface places a fundamental limit on the accuracy of chemical sensing (2), regardless of its sensor's molecular details. Since then, theoretical works have studied the effects of receptor binding (26–28), maximum-likelihood estimation (29), energy consumption with noisy readout molecules (10,30–32), time-varying concentrations (11,33,34), constant concentration ramps (8,35,36), and other factors (28,37) on this fundamental limit. Furthermore, several studies have argued that the sensitivity of bacteria's chemosensing apparatus approaches the molecule-counting limit (2,8). However, it is still unclear whether this fundamental limit meaningfully constrains the information *E. coli* get about chemical signals, and thus their speed at climbing gradients. Answering this question has been challenging because it has been unclear how the fidelity of chemosensing relates to chemotaxis performance, and because of difficulties with measuring, quantifying, and interpreting cells' internal encoding of external signals.

Here, we address these challenges with a combination of information theory and single-cell FRET measurements. Information theory allows us to quantify the fidelity of signal encoding in a cellular system, and single-cell FRET measurements give us a direct readout of the kinase activity in which *E. coli* encode environmental information. We first derive the physical limit on the rate at which an ideal sensor can acquire behaviorally-relevant information, set by ligand arrival noise. Next, we derive the rate at which *E. coli* encode this information in their kinase activity. By measuring signal statistics, kinase response functions, and fluctuations in kinase activity, we quantify both the physical limit and how much information a typical *E. coli* cell gets during chemotaxis. We find that *E. coli* get orders of magnitude less information than the physical limit. Therefore, when signals are weak and sensor quality matters, cells climb gradients much slower than an ideal, single-molecule-sensing agent could. Our work opens up new questions about what costs, constraints, or competing objectives prevent them from being closer to the physical limit.

Chemotaxis requires information about the current time derivative of concentration

Determining whether particle arrival noise is a limiting factor during *E. coli* chemotaxis presents conceptual challenges. Cells process measurements of their chemical environment into internal states, like the activity of kinases and the concentrations of signaling molecules. However, the goal of the chemotaxis system is not to represent the current concentration with high accuracy per se, but instead to utilize the concentration signal to move up a chemical gradient. Thus, cells need to capture certain aspects of signals that are behaviorally-relevant, but not necessarily in a format which is simply interpretable to an observer. To quantify how accurate such internal representations are thus requires a mathematical understanding of what features of the concentration signal are relevant to chemotaxis.

Our approach for addressing this builds on our recent work (1), where we identified the behaviorally-relevant information for *E. coli* chemotaxis. In particular, we showed that the amount of such information that the cell uses at the motor *determines* its gradient-climbing speed, $v_d \propto \left(\dot{I}\right)^{1/2}$. Furthermore, due to the data-processing inequality (38,39), the amount of this information in any intermediate variable *bounds* performance (see also SI). The key chemical signal that the cell needs to encode is the (relative) rate of change of concentration, $s(t) = \frac{d}{dt}\log(c)$ (Fig. 1). Then, the behaviorally-relevant information is the "transfer entropy rate" (40) from *current* signal, $s(t)$, to a time-dependent variable $x(t)$ that encodes the signal in its trajectory, $\{x\}$, up to time t:

$$\dot{I}^*_{s\to x} \equiv \lim_{dt\to 0} \frac{1}{dt} I(x(t+dt); s(t)|\{x\}), \tag{1}$$

where $I(X;Y|Z)$ is the mutual information between X and Y, conditioned on Z (38,41). Importantly, the current value of $x(t)$ does not need to be an explicit representation of $s(t)$; it just has to carry information about $s(t)$ in its trajectory.

This points to a way of quantifying how molecule-counting noise limits behaviorally-relevant information for chemotaxis, and how *E. coli* compare to the limit. The stochastic arrival rate of ligand molecules at the cell surface, $r(t)$, is the first quantity that a cell can physically measure that encodes information about signals $s(t)$ (Fig. 1). Thus, the transfer entropy rate $\dot{I}^*_{s\to r}$ (i.e. with $x = r$ in Eqn. 1) is a fundamental physical limit on the sensory information available for chemotaxis. An ideal agent would make navigation decisions based on a perfect readout of past particle arrivals $\{r\}$, but this process would still be noisy due to their inherent stochasticity. Then, *E. coli* encodes the signal in the activity of CheA kinases, $\{a\}$, from which downstream behavioral decisions are made. The data-processing inequality implies that $\dot{I}^*_{s\to r} \geq \dot{I}^*_{s\to a}$. Therefore, to compare *E. coli* to the physical limit, we must quantify the information about $s(t)$ encoded in $\{a\}$, $\dot{I}^*_{s\to a}$ (i.e. with $x = a$ in Eqn. 1). If $\dot{I}^*_{s\to a}$ is comparable to $\dot{I}^*_{s\to r}$, then *E. coli*'s signaling pathway acquires most of the information that is available in molecule arrivals. This comparison would allow us to determine whether *E. coli*'s chemotaxis performance is limited by the external physics of ligand diffusion or by other factors.

Our task now is to obtain closed form expressions for $\dot{I}^*_{s\to r}$ and $\dot{I}^*_{s\to a}$, and then quantify them with experimental measurements. In the SI (Eqn. 10), we show that this transfer entropy rate is equivalent to a *predictive* information rate (42–48),

$$\dot{I}^*_{s\to x} = -[\partial_\tau I(s(t+\tau); \{x\})]_{\tau=0}. \tag{2}$$

On the right, τ is a time interval into the future at which the signal $s(t+\tau)$ is predicted from past observations, $\{x\}$, making this a predictive information. Thus, the information about current signal $s(t)$

that is *encoded* in past x is the same as the accuracy with which $s(t)$ can be *estimated* from past x. We used this form to derive expressions for $\dot{I}^*_{s\to r}$ and $\dot{I}^*_{s\to a}$ (SI). Fig. 1 illustrates this problem, showing simulated time traces of signal s, particle arrival rate r, and kinase activity a. The goal of a chemotaxing *E. coli* is to construct an optimal running estimate of $s(t)$. An ideal agent does this from observations $\{r\}$, whereas the cell only has access to past kinase activity $\{a\}$.

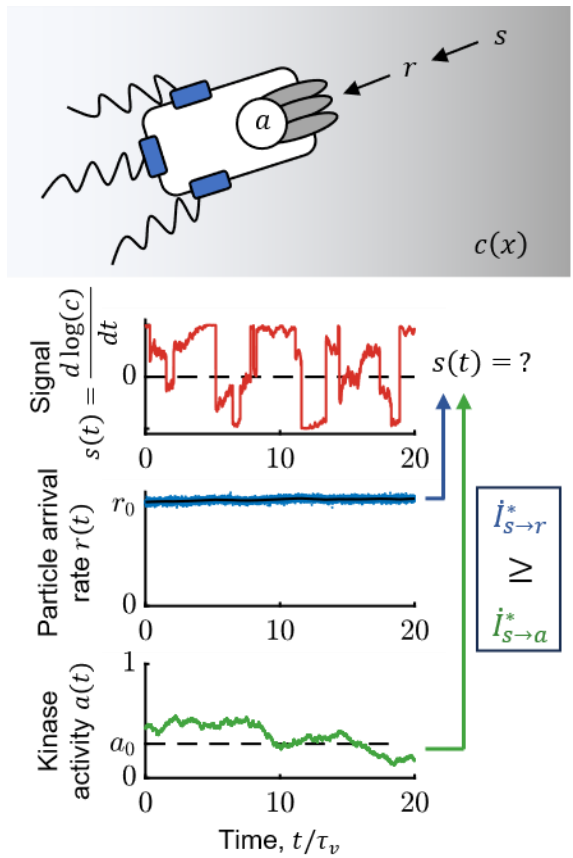

Figure 1: *E. coli* need to infer rate of change of attractant concentration from stochastic molecule arrivals. Top: Bacteria do not measure signal $s = \frac{d}{dt}\log(c)$ directly—instead, they can at best measure stochastic particle arrivals at rate $r(t)$ at their transmembrane receptors. Receptor-associated kinases respond to ligand arrivals with changes in activity, $a(t)$, and encode information about $s(t)$, but also introduce additional noise. Bottom: Simulated traces of $s(t)$ (red); $r(t)$ (blue); $\langle r(t)\rangle = k_D\, c(t)$ (black); and kinase activity $a(t)$ (green) for a cell exhibiting run-and-tumble motion in a shallow chemical gradient. r_0 is the background particle arrival rate, $r_0 = k_D\, c_0$, and a_0 is the baseline level of kinase activity. The cell's task is to infer $s(t)$ from kinase activity a, and the fidelity of this inference is quantified by the transfer entropy rate, $\dot{I}^*_{s\to a}$. An ideal agent would directly estimate $s(t)$ from the particle arrival rate r, without the noise in kinase activity, thus setting the physical limit, $\dot{I}^*_{s\to r}$. The simulation above was performed in a background concentration $c_0 = 1\ \mu\mathrm{M}$ and gradient of steepness $g = 0.3\ \mathrm{mm}^{-1}$.

Physical limit on information due to stochastic particle arrivals

We first derive an expression for the physical limit, $\dot{I}^*_{s\to r}$, from a model for the dynamics of $s(t)$ and $r(t)$. In static gradients, the signals a cell experiences are determined by their own motion in the gradient. Accordingly, in a gradient of steepness $g = d\log(c)/dx$, the signal is $s(t) = g\, v_x(t)$, where v_x is the cell's up-gradient velocity. As done previously (1,48), we consider a cell exhibiting run-and-tumble motion in a shallow gradient. In this regime, to leading order in g, the information rate only depends on the correlation function of up-gradient velocity in the absence of a gradient, $V(t)$, since s is proportional to g. Thus, we approximate the signal as Gaussian, and its dynamics are fully characterized by the following correlation function:

$$\langle s(t)\, s(t')\rangle = g^2\, V(t-t') = g^2\, \sigma_v^2 \exp\left(-\frac{|t-t'|}{\tau_v}\right). \tag{3}$$

Here, $V(t)$ is the correlation function of v_x, σ_v^2 is the variance v_x, and τ_v is the signal correlation time, which depends on the cell's mean run duration, the persistence of tumbles, and rotational diffusion (1,49).

We take particle arrival events to follow a Poisson process with time-varying rate $\langle r(t)\rangle = 4\, D\, l\, c(t) = k_D\, c(t)$, where D is the diffusivity of the ligand and l is the diameter of a circular patch on the cell's surface (2,28). If a sufficient number of particles arrive per run, $r_0\, \tau_v \gg 1$, which is valid in our experimental conditions, we can approximate the number of particles that arrive per unit time as Gaussian:

$$r(t) = k_D\, c(t) + \sqrt{r_0}\;\xi(t). \tag{4}$$

Here, $r_0 = k_D\, c_0$ is the background molecule arrival rate, where c_0 is the background concentration, and the noise is $\langle \xi(t)\, \xi(t')\rangle = \delta(t-t')$.

Next, since $s(t)$ and $\{r\}$ are each approximately Gaussian, the mutual information between them in Eqn. 2 has a known form (38) (SI Eqn. 13). In particular, it depends on $\sigma^2_{s|r}(\tau)$, the variance of the optimal estimate of $s(t+\tau)$ constructed from the past of r. Thus, the problem of deriving the physical limit reduces to solving $\sigma^2_{s|r}(\tau)$, which can be done using causal Wiener filtering theory (50–52) (see also (44,48,53–55)) (SI). In the SI, we derive the physical limit on behaviorally-relevant information for chemotaxis, which in the limit of shallow gradients reduces to:

$$\dot{I}^*_{s\to r} \approx \frac{1}{\tau_v}\frac{1}{4}\gamma_r. \tag{5}$$

Above, we have defined the dimensionless signal-to-noise ratio of particle arrivals, $\gamma_r = 2\, r_0\, g^2\, \sigma_v^2\, \tau_v^3$. Eqn. 5 is valid when $\gamma_r \ll 1$, which defines the small-signal regime for $\dot{I}^*_{s\to r}$. We also provide a full expression for $\dot{I}^*_{s\to r}$ in the SI (Eqn. 44). The signal strength is proportional to r_0^2, while the noise is proportional to r_0. Thus, increasing the molecular arrival rate r_0, the gradient steepness g, or the variance of the up-gradient swimming speed σ_v increases the signal-to-noise ratio of particle arrivals. Furthermore, the longer the cell maintains its heading, τ_v, the more time it has to average out the noise of particle arrivals. Past work has shown that the relative error of estimating a constant time derivative scales as $1/T^3$, where T is the integration time (35). In chemotaxis, the longest reasonable integration time is the time scale on which the signal doesn't change significantly, τ_v. Therefore, a factor of τ_v^3 appears in γ_r. The derivation of $\dot{I}^*_{s\to r}$ also provides the optimal kernel for constructing a running estimate of $s(t)$ given past particle arrivals $\{r\}$, which we discuss in the SI (Fig. S4).

Above, we have modeled an ideal sensor that "absorbs" every molecule it senses (2). If the sensor cannot distinguish between new ligand arrival events and rebinding events, the bound is lower by an order-1 prefactor (28,37).

Information encoded in *E. coli*'s CheA kinase activity

How do *E. coli* compare to the fundamental limit? To answer this, we need to derive and experimentally quantify the information, $\dot{I}^*_{s\to a}$, encoded in the activity $a(t)$ of *E. coli*'s CheA kinases. This in turn requires models for both noise and responses of kinase activity.

As done before (1), in shallow gradients or for small signals, kinase activity can be described using linear response theory. In background particle arrival rate r_0 and with steady-state kinase activity a_0, then activity becomes:

$$a(t) = a_0 - \int_{-\infty}^{t} K_r(t-t')\,(r(t') - r_0)\,dt' + \eta_n(t). \tag{6}$$

E. coli respond to a step increase in attractant concentration with a fast initial drop in kinase activity, followed by slow adaptation back to pre-stimulus levels (56). This response is captured by a phenomenological form for the response function:

$$K_r(t) = G_r\left(\left(\frac{1}{\tau_1}+\frac{1}{\tau_2}\right)\exp\left(-\left(\frac{1}{\tau_1}+\frac{1}{\tau_2}\right)t\right) - \frac{1}{\tau_2}\exp\left(-\frac{t}{\tau_2}\right)\right)\Theta(t), \tag{7}$$

where G_r is the gain of the response to particle arrival rate r, τ_1 is the fast initial response time, τ_2 is the slow adaptation time, and $\Theta(t)$ is the Heaviside step function. This response function can equivalently be expressed in terms of responses to past signals s, with a related kernel $K(t)$ that we used previously (1) ($K_r(t) = \frac{1}{r_0}\frac{d}{dt}K(t)$; Methods, Eqn. 15 below).

Noise in kinase activity is driven by a combination of stochastic particle arrivals and internally-driven fluctuations. Single-cell experiments have observed large, slow fluctuations in kinase activity on a time scale of 10 s (1,57–59). These are well-described as Gaussian, $\eta_n(t)$ in Eqn. 6, with correlation function:

$$\langle \eta_n(t)\,\eta_n(t')\rangle = D_n\,\tau_n\,\exp\left(-\frac{|t-t'|}{\tau_n}\right). \tag{8}$$

Here, D_n is the diffusivity of slow noise in kinase activity, and τ_n is its correlation time. So far, it has not been possible to measure noise in kinase activity at time scales near or below τ_1, but the noise cannot go below the level set by kinase responses to particle arrival noise. Thus, we construct a phenomenological noise model that agrees with experiments at low frequencies while obeying known physics at high frequencies. This consists of adding kinase responses to particle shot noise in Eqn. 4 to the slow fluctuations in Eqn. 8. Due to the adaptive nature of the signaling pathway, all the parameters that appear in the above Eqns. 7 and 8 can depend on the background particle arrival rate, r_0.

With this model, we can derive an expression for the information about signal encoded in kinase activity, $\dot{I}^*_{s\to a}$. As above, this reduces to deriving $\sigma^2_{s|a}(\tau)$, the variance of the signal $s(t+\tau)$ reconstructed from the past of kinase activity $\{a\}$, which can again be solved using Wiener filtering theory (SI). Furthermore,

209 previous measurements (and measurements below) have shown that $\tau_1 \ll \tau_v$ (1,60,61) and $\tau_2 \approx \tau_n$ (1).
210 Thus, in shallow gradients, we find that the information rate to kinase activity is:

211 $$\dot{I}^*_{s\to a} \approx \frac{1}{\tau_v}\frac{1}{4}\,\gamma_a \frac{\gamma_r/\gamma_a}{\left(1+\sqrt{\gamma_r/\gamma_a}\right)^2}. \tag{9}$$

212 Here, we have defined the dimensionless kinase signal-to-noise ratio $\gamma_a = \frac{G_r^2}{D_n}\, r_0^2\, g^2\, \sigma_v^2\, \tau_v$ and used $\gamma_r =$
213 $2\, r_0\, g^2\, \sigma_v^2\, \tau_v^3$ from above. Eqn. 9 is valid when $\gamma_a \ll 1$, which defines the small-signal regime for $\dot{I}^*_{s\to a}$. We
214 also provide a full expression for $\dot{I}^*_{s\to a}$ in the SI (Eqn. 89). An ideal cell with no internal noise sources would
215 operate at the physical limit, Eqn. 5, corresponding to infinite signal-to-noise in kinase activity, $\gamma_a \to \infty$.
216 Taking this limit in Eqn. 9 results in the expression for $\dot{I}^*_{s\to r}$ above (Eqn. 5). Conversely, a cell with internal
217 noise would degrade information about the signal, and in the limit of large noise would have an
218 information rate given by $\dot{I}^*_{s\to a} \approx \frac{1}{\tau_v}\frac{1}{4}\,\gamma_a$. The derivation of $\dot{I}^*_{s\to a}$ also provides the optimal kernel for
219 constructing a running estimate of $s(t)$ from past kinase activity $\{a\}$, which we discuss in the SI.

220 To compare the information *E. coli* get during chemotaxis to the physical limit, we must quantify $\dot{I}^*_{s\to a}$ and
221 $\dot{I}^*_{s\to r}$ by measuring the parameters above from live cells.

222

223 **Single-cell measurements constrain signal and kinase properties**

224 Next, we use single-cell tracking and FRET experiments to measure the parameters that characterize the
225 signal statistics, kinase response function, and kinase noise statistics in multiple background
226 concentrations of attractant. As the attractant, we used aspartate (Asp), to which the *E. coli* chemotaxis
227 signaling pathway responds with the highest sensitivity among known attractants (62).

228 To quantify the parameters describing cell swimming statistics (Eqn. 3), and thus the signal statistics, σ_v^2
229 and τ_v, we recorded trajectories of cells swimming in multiple uniform background concentrations of Asp:
230 $c_0 =$ 0.1, 1, and 10 μM (Fig. 2A). Single cells in the clonal population exhibited a range of swimming
231 behaviors (57,63–69); thus, as before (1), we focus on cells with median values of the phenotypic
232 parameters. We binned cells by the fraction of time they spent in the "run" state, P_{run}, and computed the
233 velocity correlation function, $V(t)$, among cells with the median P_{run}. The parameters σ_v^2 and τ_v in each
234 background c_0 were then inferred by fitting the correlation functions with the decaying exponential in
235 Eqn. 3. These parameters depended weakly on c_0, and their values in $c_0 = 1$ μM Asp were $\sigma_v^2 = 146 \pm$
236 $5\ (\mu m/s)^2$ and $\tau_v = 1.19 \pm 0.01\ s$ (see Fig. S1AB for their values in all backgrounds).

237 We measured kinase response functions as before (1), using a microfluidic device in which we can deliver
238 controlled chemical stimuli with high time resolution (~100 ms) (70). Cells immobilized in the device were
239 delivered ten small positive and negative step changes of Asp concentration around multiple backgrounds
240 c_0 (Fig. 2B; Methods). Kinase responses were measured in single cells through FRET (58,59,70–74)
241 between CheZ-mYFP and CheY-mRFP. Then we fit each cell's average response with the phenomenological
242 response function $K_r(t)$ in Eqn. 7, and computed the population-median parameter values. However, τ_1
243 estimated this way includes the dynamics of CheY-CheZ interactions, which are slower than the fast time
244 scale of the kinases. We used $\tau_1 = 0$ for calculations below, which slightly overestimates the information
245 rate $\dot{I}^*_{s\to a}$, making this a conservative choice in estimating where cells are relative to the bound. The

adaptation time τ_2 depended weakly on c_0 (in $c_0 = 1\ \mu\text{M}$, $\tau_2 = 7.4 \pm 0.3\ s$) (Fig. S1D), but G_r varied significantly with c_0: for $c_0 = \{0.1, 1, 10\}\ \mu\text{M}$ we measured $G_r = \frac{1}{kD}\{3.2 \pm 0.1, 2.28 \pm 0.05, 0.251 \pm 0.009\}$ (Fig. S1EF).

The dependence of G_r on c_0 was consistent with the phenomenological Monod-Wyman-Changeux (MWC) model for kinase activity (23,75–77), which captures numerous experimental measurements (70,72–74,78). First, in the methods we note that $G_r = \frac{1}{r_0} G(c_0)$, where $G(c_0)$ is the MWC model gain (Eqn. 16 in the Methods below). The MWC model in turn predicts that $G(c_0) \approx G_\infty \frac{c_0}{c_0 + K_i}$, where K_i is the dissociation constant of two-state receptors for ligand when in their inactive state and G_∞ is a constant (Methods). Thus, in low backgrounds where $c_0 \ll K_i$ the cell is in the "linear-sensing" regime and $G_r = G_\infty \frac{1}{k_D\, K_i}$ is constant; in high backgrounds where $c_0 \gg K_i$, cells transition to the "log-sensing" regime (79–81), with gain $G_r \approx G_\infty / r_0$. Fitting $G(c_0)$ to the MWC model, we estimated that $G_\infty = 3.5 \pm 0.1$ and $K_i = 0.81 \pm 0.04\ \mu\text{M}$.

Finally, we estimated the noise parameters of slow kinase fluctuations by measuring kinase activity in single cells experiencing constant Asp concentrations c_0 (Fig. 2C). The diffusivity D_n and time scale τ_n of slow fluctuations in Eqn. 8 were extracted from these time series using Bayesian filtering (1,82) (Methods). We then computed the population-median parameter values. Both of these parameters depended weakly on c_0, and their values in $c_0 = 1\ \mu\text{M}$ were $D_n = 8.1 \pm 0.9 \times 10^{-4}\ s^{-1}$ and $\tau_n = 8.7 \pm 0.9\ s$ (see Fig. S1CD for their values in all backgrounds).

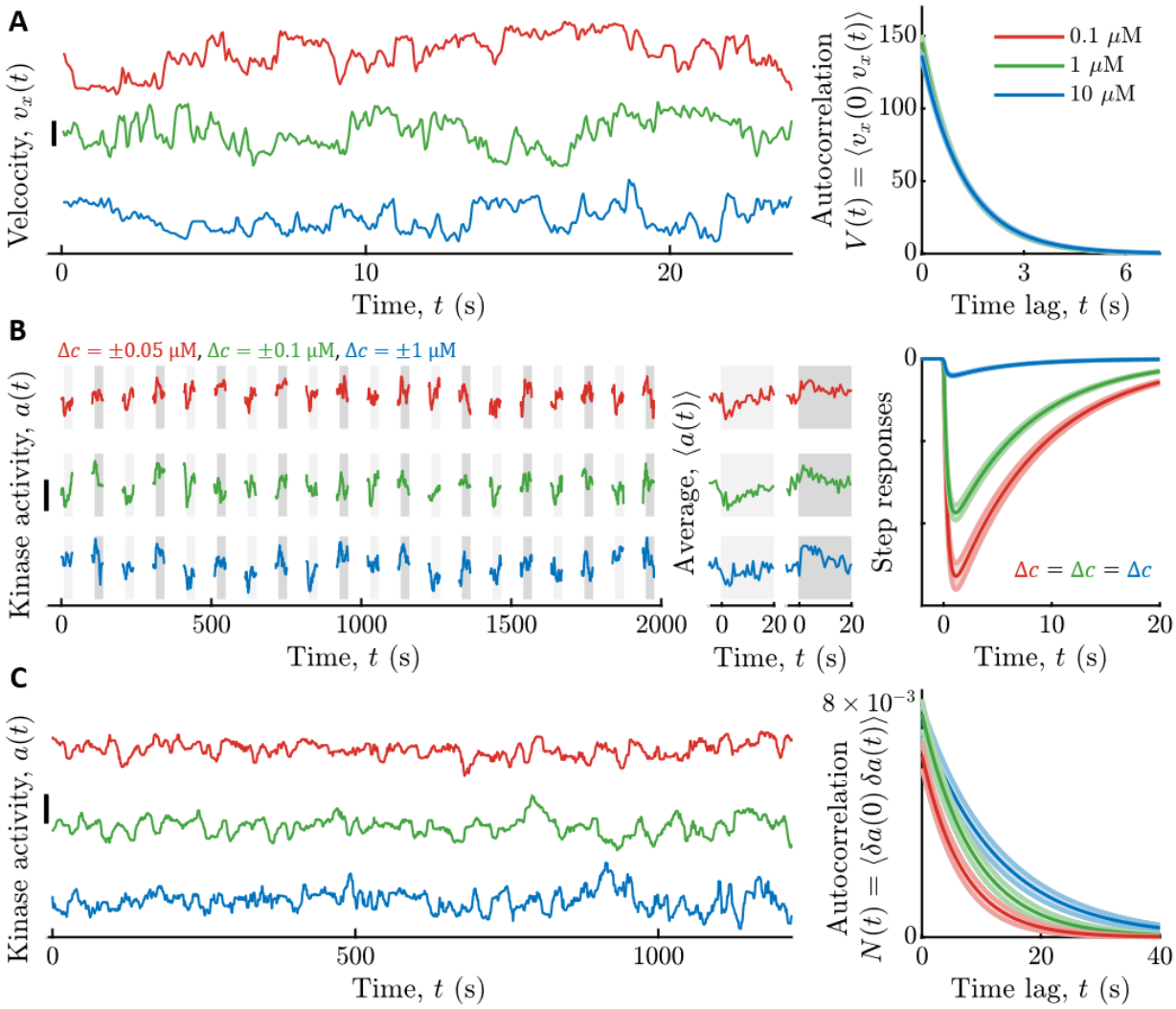

Figure 2: Measured signal statistics and kinase responses and fluctuations in different background ligand concentrations. **A)** Signal statistics. Left: Representative time series of up-gradient velocity v_x from three individual cells are shown, one in each background concentration c_0. Scale bar is 20 μm/s. Cells were binned by the fraction of time they spend running, P_{run}, and the velocity autocorrelation function was computed by averaging over cells in the median bin ($P_{run} \approx 0.89$). The parameters of the velocity autocorrelation function were then fit with a decaying exponential $V(t) = \sigma_v^2 \exp\left(-\frac{t}{\tau_v}\right)$ to extract the velocity variance σ_v^2 and correlation time τ_v. Right: Model fits for velocity autocorrelation functions are shown for each c_0. The curves are on top of each other. Units on the y-axis are (μm/s)^2. Throughout, line colors indicate c_0: Red: 0.1 μM Asp; Green: 1 μM Asp; Blue: 10 μM Asp, and shading is standard error of the mean (SEM). **B)** Linear responses. Left: Immobilized cells were continuously exposed with a constant background concentration c_0 of aspartate (Asp). The fraction of active kinases (kinase activity) was measured by FRET in blocks of 25 seconds, separated by 65 seconds without illumination. In each block, after 5 s, concentration was stepped up (light gray shading) or down (dark gray shading) around c_0, then maintained for 20 s, and then returned to c_0. Concentration step sizes Δc were different for each c_0 (shown above the panel). Shown are three representative cells, one from each c_0. Scale bar is 0.3. Middle:

Average responses of the cells in the left panel to a step up (light gray) and step down (dark gray) of concentration. Single-cell responses were fit to the model in Eqn. 15 to extract single-cell parameters of the response function $K_r(t)$. Right: Using the median parameter values of the population, shown are model fits for kinase responses to a step increase in concentration of size Δc, for each background c_0. The gain of the response G_r decreases with c_0. **C)** Noise statistics. Left: Fluctuations in kinase activity were measured in constant background concentrations. Representative time series from three cells are shown, one in each background concentration. Scale bar height is 0.3. Parameters of the slow noise autocorrelation function (Eqn. 8), were fit to single-cell traces using Bayesian filtering (SI). Right: Estimated noise autocorrelation functions for the median cell are shown, for each background concentration c_0. Units on the y-axis are kinase activity squared.

Comparing *E. coli* to the physical limit

We can now answer our central question: does the stochastic arrival of particles prevent *E. coli* from getting more information during chemotaxis? The remaining unknown needed to answer this is the diffusion-limited particle arrival rate constant, $k_D = 4\,D\,l$. We take $l = 60\ \mathrm{nm}$ (82) as a conservative lower estimate of the diameter of the receptor array and $D = 800\ \mu\mathrm{m}^2/\mathrm{s}$ (83,84) as the ligand diffusivity. With these, we estimate that $k_D \approx 1.2 \times 10^5\ \mathrm{s}^{-1}\ \mu\mathrm{M}^{-1}$, indicating that about 10^5 independent molecules strike the cell's receptor array per second in a background of $c_0 = 1\ \mu\mathrm{M}$, which is comparable to previous estimates (2,8).

Both *E. coli*'s information rate, $\dot{I}^*_{s\to a}$, and the physical limit, $\dot{I}^*_{s\to r}$, are approximately proportional to the gradient steepness squared, g^2 in the limit of a shallow gradient (black lines in Fig. 3AB). Therefore, we quantify the information rates per g^2, using the parameters measured in the previous section. In particular, we plot the full expressions for the information rates, which are given in the SI. In Fig. 3A, we plot these quantities as functions of background concentration c_0, for varying values of the gradient steepness $g \in [0, 0.4]\ \mathrm{mm}^{-1}$, within which we observed linear dependence of chemotaxis drift speed on g (1). Doing so reveals that *E. coli* are surprisingly far from the physical limit: in shallow gradients, $\dot{I}^*_{s\to a}$ is at least two orders of magnitude below $\dot{I}^*_{s\to r}$ across all background concentrations.

To quantify the fidelity of *E. coli*'s chemical sensing relative to the physical limit, we computed the ratio of *E. coli*'s information rate relative to the physical limit, $\eta \equiv \frac{\dot{I}^*_{s\to a}}{\dot{I}^*_{s\to r}}$. We first focus on the limit of vanishingly small gradients, where η is independent of g, and we plot it in Fig. 3B (black) as a function of background concentration, c_0. In low backgrounds, $c_0 \ll K_i$, the kinase signal-to-noise ratio, γ_a, scales as c_0^2 since *E. coli*'s gain G_r and noise in kinase activity are constant. Thus, *E. coli*'s information rate scales as $\dot{I}^*_{s\to a} \propto c_0^2$. Since the physical limit scales as $\dot{I}^*_{s\to r} \propto c_0$, we get $\eta \propto c_0$, which goes to zero with decreasing background concentration. In high backgrounds, $c_0 \gg K_i$, the kinase signal-to-noise ratio γ_a is approximately constant because the gain depends on background concentration as $G_r \propto 1/c_0$, which cancels the concentration-dependence of the molecular arrival rate, $r_0 \propto c_0$, and so $\dot{I}^*_{s\to a}$ is constant. As a result, we get $\eta \propto 1/c_0$, which again goes to zero with increasing concentration. These two regimes are separated by a peak at $c_0 = K_i$, where $\eta \approx 0.014 \pm 0.002$ at our closest measured data point (black in Fig. 3B). In this

background, the variance of filtered particle arrival noise is largest, but it is still much smaller than the variance of other kinase noise sources (see Figs. S1, S3).

For small but finite gradients, we find that η increases as the gradient g gets steeper, increasing to $\eta \approx 0.1$ when $g = 0.4\ \mathrm{mm}^{-1}$. This smaller value of η does not imply that *E. coli* count every particle in steeper gradients. Instead, η increases with g because the information rate, $\dot{I}^*_{s\to r}$, saturates in steeper gradients (solid color lines decreasing with g in Fig. 3A). In a steep gradient, even a poor sensor can accurately infer the signal, $s(t)$, and increasing particle counts only provides marginal gains on the information rate. Mathematically, this can be seen through the weak dependence of $\dot{I}^*_{s\to r}$ on g outside of the small-signal regime (Fig. 3A). $\dot{I}^*_{s\to a}$, on the other hand, remains roughly proportional to g^2 to much steeper gradients. Thus, kinase activity is still in the small-signal regime in conditions where particle arrivals are not. In steeper gradients where signal can be reconstructed accurately, *E. coli* are able to get closer to the information bound even with a sensor that is far from counting every particle.

We support this further in Figs. 3CD. In Fig. 3C, we show the power spectrum of total noise in kinase activity (green line) compared to the power spectrum of filtered particle arrival noise (blue line). If *E. coli* were close to the particle-counting limit, nearly all noise in kinase activity would come from filtering particle arrivals; instead, kinase fluctuations are much larger over the range of frequencies observable in experiment (Fig. 3C, outside the pink region). We extrapolate to higher frequencies by conservatively assuming that the lines approach each other (black line), but it is possible that there are additional high frequency noise sources (putting the black line higher in shaded region of Fig 3C) or that the response function has a slower τ_1 than in our model (putting the blue line lower in pink shaded region of Fig 3C). The information rate is relatively insensitive to these choices (see SI Fig S3 for discussion). In Fig. 3D, we show the optimal reconstructions of $s(t)$ in Fig. 1, both from past particle arrivals $\{r\}$ and from past kinase activity $\{a\}$ using the parameter values determined from the experiments. The fidelity of the reconstruction from kinase activity is visibly worse than that from particle arrivals, consistent with the much lower information about the signal encoded in the kinase activity. Thus, *E. coli*'s information about signals during chemotaxis is not limited by the physical limit set by counting single particle arrivals.

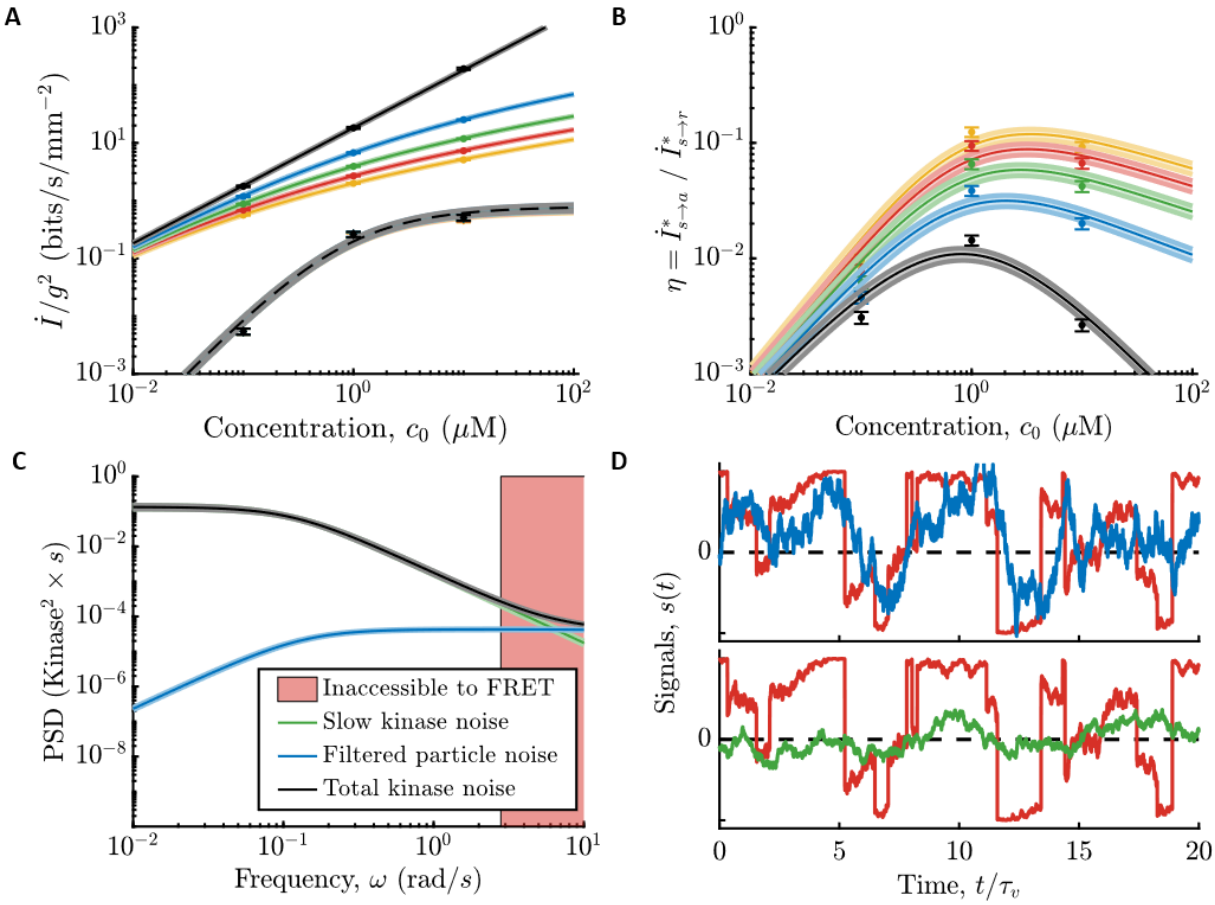

Figure 3: Comparing *E. coli*'s information rates to the particle counting limit. A) Information rates per gradient steepness squared, g^2, in particle arrivals, $\dot{I}^*_{s\to r}$ (SI Eqn. 44; solid lines), and in kinase activity, $\dot{I}^*_{s\to a}$ (SI Eqn. 89; dashed lines use Eqn. 16 and parameters measured in $c_0 = 1$ μM) for gradients of varying steepness, $g \in \{0^+, 0.1, 0.2, 0.3, 0.4\}$ mm^{-1} in black, blue, green, red, yellow, where black is the small gradient limit, $g \to 0$. Dots are experimental measurements. Error bars and shading throughout are SEM. We find that *E. coli* far from the physical limit set by particle arrivals when signals are weak and sensor quality matters. In particular, the fundamental limit $\dot{I}^*_{s\to r}$ scales slower than g^2, even for moderate g, indicating that it is out of the small-signal regime. Information in kinase activity $\dot{I}^*_{s\to a}$, on the other hand, is roughly proportional to g^2 (the lines are on top of each other), indicating that *E. coli* are still in the small-signal regime. **B)** $\eta = \dot{I}^*_{s\to a}/\dot{I}^*_{s\to r}$ versus c_0. Colors and markers are same as in (A). In steeper gradients, the quality of *E. coli*'s chemosensory apparatus matters less for getting close to the limit. **C)** Fit models for the noise power spectra in background concentration $c_0 = 1$ μM. Green: fit to measured slow noise in kinase activity. Blue: particle arrival noise filtered through kinase response kernel. Black: Sum of green and blue, used as a conservative estimate of information in kinase activity. Red shading: experimentally-inaccessible region using CheY-CheZ FRET. See also SI Fig. S3 and the SI section "Modeling kinase activity" for discussion about noise in the red region. If *E. coli* were close to the physical limit, the black line would be close to the blue line at all frequencies. Instead, excess slow noise in kinase activity dominates over the entire range of observable frequencies. **D)** *E. coli*'s low information rates relative to the physical limit correspond to poor estimates of the signal $s(t)$. Red: true signal from Fig. 1 with $c_0 = 1$ μM and $g = 0.3$ mm^{-1}. Top, blue: reconstructed signal from particle arrival rate r in Fig. 1, using the optimal causal kernel (SI Eqn. 57).

Bottom, green: reconstructed signal from kinase activity a in Fig. 1, using the optimal causal kernel (SI Eqn. 95).

Discussion

Here, we studied how the physics of chemosensing (2) limits *E. coli*'s ability to encode information about signals relevant for chemotaxis. We derived a physical limit on information about the current time derivative of concentation, which we previously showed cells need for chemotaxis (1), by considering an ideal sensor able to register the arrival of every particle at its surface. We then measured the rate at which *E. coli* encode this information into the activity of their receptor-associated kinases through a series of single-cell measurements in multiple background concentrations of attractant. We found that *E. coli* are far from the physical limit of an idealized sensor, getting only a few percent of the information available in ligand particle arrivals in shallow gradients. Thus, the fidelity of *E. coli*'s chemosensing, and hence their chemotaxis performance, is not limited by the physics of molecule counting.

Previous work anticipated that *E. coli* would be much closer to the particle counting limit. Berg and Purcell argued that, in *E. coli* and *Salmonella typhimurium* chemotaxis, the change in concentration over a single run in a typical gradient could be estimated by an ideal agent with uncertainty smaller than the mean (2). From this, they concluded that the bacterial chemotaxis machinery is nearly optimal. However, their calculation does not imply that bacteria actually achieve that level of accuracy. Ref. (8) fit agent-based simulations to experimental measurements of *Vibrio ordalii* climbing dynamic chemical gradients and argued that this bacterium is within a factor of ~6 of the particle counting limit. However, this analysis assumed that cells infer $s(t)$ in short, independent time windows of duration $T = 0.1\ s$. Instead, real cells continuously monitor new particle arrivals and forget old ones, allowing them to average out molecule counting noise for integration times up to the signal correlation time τ_v. This increases the theoretical maximum precision in the analysis of Ref. (8), and thus *V. ordalii*'s distance from the limit, by a factor of $(\tau_v/T)^3 = \left(\frac{0.45\ s}{0.1\ s}\right)^3 \sim 90$, due to the T^3 in the uncertainty about signal (35). We believe this explains the discrepancy between our findings. It also suggests that similar constraints might limit the sensing fidelity of *E. coli* and other bacterial species.

We discovered a new relationship between two previously-disconnected information quantities: the transfer entropy rate (40) and the predictive information (42). While past work has argued that signaling networks should carry predictive information (12,13,42,44,45), here we identify a specific behavior where performance depends quantitatively on a predictive information rate. This new predictive information rate allows us to distinguish two possible sources of inefficiency that we could not separate in our previous study (1). First, kinases could encode information about past signals s, which do not contribute to gradient climbing; and second, relevant information could be lost in communication with the motors. Using $\dot{I}^*_{s\to a}$ derived here, which isolates information about the present signal, we estimate that about 90% or more of the cell's information rate to kinase activity is relevant to chemotaxis, depending on c_0 (see SI), implying that the remaining losses are in communication with the motor.

Our analysis has implications for how we think about intermediary variables in signal transduction pathways. While behavioral decisions often require information about a current (or possibly future)

408 external signal, intermediate variables do not need to represent these in their current value. For
409 example,the entire past trajectory of kinase activity, $\{a\}$, contains more information than its current value,
410 a, about the current signal, s. This information can be extracted by downstream processing, all the way
411 down to the motors (see SI section "Optimal kernel for estimating signal from kinase activity"). The
412 information available to downstream processing is quantified by the predictive information rate, and
413 critically, this quantity is agnostic to that processing. Here we took advantage of this property to measure
414 the fidelity of the kinases without assuming their activity is an instantaneous, noisy readout of signal.

415 Why are *E. coli* so far from the particle counting limit? It may be that design constraints prevent them
416 from reaching this limit. *E. coli* must be able to perform chemotaxis over many orders of magnitude in
417 background concentration, which might impose trade-offs that prevent the system from achieving
418 optimality. Fold-change detection enables this (79–81), but also causes *E. coli*'s gain, G_r, to decrease with
419 increasing concentration (Methods). Thus, just to keep η from decreasing with c_0, *E. coli* would need to
420 have kinase noise variance that decreases with concentration like $1/c_0$. Instead, we find that it is roughly
421 constant. Suppressing fluctuations or amplifiying signals generally requires spending energy or resources
422 (10–16,86,87), and those costs might not be worth the fitness benefit in this case. The mechanism of
423 amplification is not well understood, but recent work has argued that it consumes energy (87–89). Thus,
424 energetic and mechanical constraints might provide currently-unknown bounds on *E. coli*'s sensory
425 fidelity.

426 Surely, *E. coli* have evolved under selection pressures other than climbing shallow gradients of aspartate.
427 *E. coli* need to sense multiple ligands, such as amino acids, sugars, and peptides (62,90), some of which
428 require different receptor types. But the presence of multiple receptor types in the receptor array reduces
429 the cooperativity to any one ligand (74), while likely still contributing to signaling noise. *E. coli* may be
430 under selection pressure not only to climb gradients but also to stay close to concentration peaks
431 (18,19,92,93). Furthermore, we do not know the typical gradient steepness they have been selected to
432 climb effectively. In an infinitely shallow gradient, we showed that an ideal sensor would allow a bacteria
433 to climb gradients at least 10 times faster than typical *E. coli* (due to $I^*_{s\to a}/I^*_{s\to r} \approx 0.01$ and $v_d \propto (I^*_{s\to a})^{1/2}$
434 (1)). However, in steeper gradients, where even a poor sensor can adequately measure direction, these
435 gains would be far smaller. For example, in a relatively steep 500-micron gradient and background of $1\ \mu\mathrm{M}$
436 of attractant, we estimate that a typical cell would get ~37% of the relevant information available to an
437 ideal sensor, and could climb ~60% as fast. It may be that the typical gradients that have driven the
438 evolution of *E. coli's* sensory apparatus are sufficiently steep as to obviate the need for an ideal single-
439 molecule sensor. In the laboratory, the amino acid gradients *E. coli* perceive when migrating collectively
440 are typically of order ~1 mm (93), and theory predicts that they can be steeper in semisolid agar (94,95)
441 in which our laboratory strain of *E. coli* was selected for chemotaxis (96–98).

442 Existing findings give qualitative support for the idea that *E. coli* are not at the fundamental limit. Berg
443 and Purcell's original paper argued that by evenly-distributing small, sparse receptors on its surface, a cell
444 can make its ligand sensor nearly as effective as if its entire surface were covered with receptors (2). Thus,
445 a chemosensor limited primarily by the noise of single particle arrivals would want to spread a limited
446 receptor budget evenly over the cell surface to maximize the rate at which unique particles are counted.
447 Instead, bacterial chemoreceptors are clustered in densely-packed arrays. This dense packing, which
448 appears to be universal across species (99), might be necessary for bacteria to integrate and amplify signal
449 that must be communicated to the motor to make all-or-none behavioral decisions.

Future experiments could probe whether hard constraints prevent *E. coli* from being close to the physical limit, or if tradeoffs would allow a cell to do better, perhaps at the cost of increased energy expenditure. This could be done by measuring information rates in single cells, where cell-to-cell variability (63,66–68,70,72,78,101,102) might enable some cells to be closer to the physical limit by chance.

While *E. coli* do not achieve the particle counting bound, their sensory capabilities are impressive. In the log-sensing regime they aquire and communicate information to the motor at a rate equivalent to an ideal sensor able to count several thousand particles every second. While current modeling efforts in chemosensing have mostly focused on quantitatively describing experimental observations, this work opens up new possibilities for a reverse engineering perspective. Our work highlights the need to understand how these systems achieve the signal processing, bandwidth, and fidelity needed for behavior, and how physical, geometric, and energetic constraints have shaped their evolution.

Methods

<u>Modeling of average kinase responses to past signal versus past particle arrival rate</u>

In our previous work (1), we modeled responses of kinase activity to past signals s instead of past particle arrival rate r. These two descriptions are equivalent in the regime of shallow gradients. We show this below by starting from average responses of kinase activity to particle arrival rate:

$$\langle a(t)\rangle = a_0 - \int_{-\infty}^{t} K_r(t-t')\,(\langle r(t')\rangle - r_0)\,dt'\,, \tag{10}$$

where angled brackets indicate averaging over repeated presentation of the same signal trajectory $\{s\}$, and thus they average out particle noise and kinase noise. From here, we will derive a response kernel to past signals that gives identical kinase responses.

First, we note that:

$$\langle r(t)\rangle - r_0 = k_D\,(c(t) - c_0) = r_0 \int_{-\infty}^{t} s(t')\,dt'\,, \tag{11}$$

where we used $s(t) \approx \frac{1}{c_0}\frac{dc}{dt}$ in shallow gradients.

It is convenient to transform the expressions above to Fourier space, where $\delta a(\omega) = F[\langle a(t)\rangle - a_0]$, $\delta r(\omega) = F[\langle r(t)\rangle - r_0]$, $K_r(\omega) = F[K_r(t)]$, and $F[f(t)] = \int_{-\infty}^{\infty} f(t)\,e^{i\,\omega\,t}\,dt$ is the Fourier transform. Then we have

$$\delta a(\omega) = -K_r(\omega)\,\delta r(\omega), \tag{12}$$

$$\delta r(\omega) = r_0 \frac{s(\omega)}{-i\,\omega}. \tag{13}$$

With this, we get:

$$\delta a(\omega) = -K_r(\omega)\,r_0 \frac{s(\omega)}{-i\,\omega} = -K(\omega)\,s(\omega) \tag{14}$$

481 where $K(\omega) = r_0 \frac{K_r(\omega)}{-i\,\omega}$ is the Fourier transform of the linear response function to signals. Thus, we can
482 either write down average kinase responses to particle arrival rate $r(t)$, with linear response function
483 $K_r(t)$, or responses to signals $s(t)$, with linear response function $K(t)$ (1):

484 $$K(t) = r_0 \int_0^t K_r(t')\,dt' = G \exp\left(-\frac{t}{\tau_2}\right)\left(1 - \exp\left(-\frac{t}{\tau_1}\right)\right). \quad (15)$$

485 where we have defined the MWC model gain $G = r_0\, G_r$ (23,76). Thus:

486 $$G_r = \frac{1}{r_0} G \approx \frac{1}{k_D} \frac{G_\infty}{c_0 + K_i}. \quad (16)$$

487 We can use the response function to particle arrivals, $K_r(t)$, to compute the power spectrum of particle
488 counting noise filtered through the kinase response kernel, $K_r(t)$, but expressed it in terms of the
489 response kernel $K(t)$ to signals s. Since we model particle arrival noise as shot noise, its power spectrum
490 is constant and equal to r_0. Filtering this noise through the response kernel $K_r(\omega)$ gives:

491 $$N_r(\omega) = r_0\, |K_r(\omega)|^2 = r_0 \left|\frac{-\,i\,\omega}{r_0}\, K(\omega)\right|^2 = \frac{1}{r_0}\, \omega^2\, |K(\omega)|^2. \quad (17)$$

492

493 Simulation details in Figure 1

494 Simulation time step was $dt = 3 \times 10^{-3}\, \tau_v$. Signal $s(t)$ was simulated in 2D by randomly sampling the
495 times of instantaneous tumbles, plus rotational diffusion during runs, which was implemented using the
496 Euler-Maruyama method. Average particle arrival rate $\langle r(t) \rangle$ was computed from the signal, and then
497 Gaussian noise of variance $\sqrt{r_0\, dt}$ was added to mimic shot noise. Kinase activity $a(t)$ was simulated using
498 the model in the main text (Eqn. 6), with biologically reasonable parameters (see Fig. 2).

499

500 Strains and plasmids

501 All strains and plasmids used are the same as in our recent work (1). The strain used for the FRET
502 experiments is a derivative of *E. coli* K-12 strain RP437 (HCB33), a gift of T. Shimizu, and described in detail
503 elsewhere (59,70). The FRET acceptor-donor pair (CheY-mRFP and CheZ-mYFP) is expressed in tandem
504 from plasmid pSJAB106 (59) under an isopropyl β-D-thiogalactopyranoside (IPTG)-inducible promoter.
505 The glass-adhesive mutant of FliC (FliC*) was expressed from a sodium salicylate (NaSal)-inducible pZR1
506 plasmid (59). The plasmids are transformed in VS115, a *cheY cheZ fliC* mutant of RP437 (59) (gift of V.
507 Sourjik). RP437, the direct parent of the FRET strain and also a gift from T. Shimizu, was used to measure
508 swimming statistics parameters. All strains are available from the authors upon request.

509

510 Cell preparation

511 Single-cell FRET microscopy and cell culture was carried out essentially as described previously
512 (1,59,70,72). Cells were picked from a frozen stock at -80°C and inoculated in 2 mL of Tryptone Broth (TB;
513 1% bacto tryptone, 0.5 % NaCl) and grown overnight to saturation at 30°C and shaken at 250 RPM. Cells

514 from a saturated overnight culture were diluted 100X in 10 mL TB and grown to OD600 0.45-0.47 in the
515 presence of 100 µg/ml ampicillin, 34 µg/ml chloramphenicol, 50 µM IPTG and 3 µM NaSal, at 33.5°C and
516 250 RPM shaking. Cells were collected by centrifugation (5 min at 5000 rpm, or 4080 RCF) and washed
517 twice with motility buffer (10 mM KPO4, 0.1 mM EDTA, 1 µM methionine, 10 mM lactic acid, pH 7), and
518 then were resuspended in 2 mL motility buffer, plus the final concentration of Asp. Cells were left at 22°C
519 for 90 minutes before loading into the microfluidic device. All experiments, FRET and swimming, were
520 performed at 22-23°C.

521 For swimming experiments, cells were prepared similarly. Saturated overnight cultures were diluted 100X
522 in 5 mL of TB. After growing to OD600 0.45-0.47, 1 mL of cell suspension was washed twice in motility
523 buffer with 0.05% w/v of polyvinylpyrrolidone (MW 40 kDa) (PVP-40). Washes were done by centrifuging
524 the suspension in an Eppendorf tube at 1700 RCF (4000 RPM in this centrifuge) for 3 minutes. After the
525 last wash, cells were resuspended with varying background concentrations of Asp.

526

527 Microfluidic device fabrication and loading for FRET measurements

528 Microfluidic devices for the FRET experiments (70–72) were constructed from polydimethylsiloxane
529 (PDMS) on 24 x 60 mm cover glasses (#1.5) following standard soft lithography protocols (102), exactly as
530 done before (1).

531 Sample preparation in the microfluidic device was conducted as follows. Five inlets of the device were
532 connected to reservoirs (Liquid chromatography columns, C3669; Sigma Aldrich) filled with motility buffer
533 containing various concentrations of Asp through polyethylene tubing (Polythene Tubing, 0.58 mm id,
534 0.96 mm od; BD Intermedic) (see SI of (1)). The tubing was connected to the PMDS device through stainless
535 steel pins that were directly plugged into the inlets or outlet of the device (New England Tubing). Cells
536 washed and suspended in motility buffer were loaded into the device from the outlet and allowed to
537 attached to the cover glass surface via their sticky flagella by reducing the flow speed inside the chamber.
538 The pressure applied to the inlet solution reservoirs was controlled by computer-controlled solenoid
539 valves (MH1; Festo), which rapidly switched between atmospheric pressure and higher pressure (1.0 kPa)
540 using a source of pressurized air. Only one experiment was conducted per device. *E. coli* consume Asp, so
541 all experiments below were performed with a low dilution of cells to minimize this effect. The continuous
542 flow of fresh media also helped ensured that consumption of Asp minimally affected the signal cells
543 experienced.

544

545 Single-cell FRET imaging system

546 FRET imaging in the microfluidic device was performed using the setup as before (1), on an inverted
547 microscope (Eclipse Ti-E; Nikon) equipped with an oil-immersion objective lens (CFI Apo TIRF 60X Oil;
548 Nikon). YFP was illuminated by an LED illumination system (SOLA SE, Lumencor) through an excitation
549 bandpass filter (FF01-500/24-25; Semrock) and a dichroic mirror (FF520-Di02-25x36; Semrock). The
550 fluorescence emission was led into an emission image splitter (OptoSplit II; Cairn) and further split into
551 donor and acceptor channels by a second dichroic mirror (FF580-FDi01-25x36; Semrock). The emission
552 was then collected through emission bandpass filters (F01-542/27-25F and FF02-641/75; Semrock;
553 Semrock) by a sCMOS camera (ORCA-Flash4.0 V2; Hamamatsu). RFP was illuminated in the same way as

554 YFP except that an excitation bandpass filter (FF01-575/05-25; Semrock) and a dichroic mirror (FF593-
555 Di03-25x36; Semorock) were used. An additional excitation filter (59026x; Chroma) was used in front of
556 the excitation filters. To synchronize image acquisition and the delivery of stimulus solutions, a custom-
557 made MATLAB program controlled both the imaging system (through the API provided by Micro-Manager
558 (103)) and the states of the solenoid valves.

559

560 Computing FRET signal and kinase activity

561 FRET signals were extracted from raw images using the E-FRET method (104), which corrects for different
562 rates of photobleaching between donor and acceptor molecules. In this method, YFP (the donor) is
563 illuminated and YFP emission images (I_{DD}) and RFP (the acceptor) emission images (I_{DA}) are captured.
564 Periodically, RFP is illuminated and RFP emission images are captured (I_{AA}). From these, photobleach-
565 corrected FRET signal is computed as before (1), which is related to kinase activity $a(t)$ by an affine
566 transform when CheY and CheZ are overexpressed (1,73). All parameters associated with the imaging
567 system were measured previously (1).

568 In each experiment, we first delivered a short saturating stimulus (1 mM MeAsp plus 100 µM serine (74))
569 to determine the FRET signal at minimum kinase activity, followed by motility buffer with Asp at
570 background concentration c_0. Before the saturating stimulus was delivered, the donor was excited every
571 0.5 seconds to measure I_{DD} and I_{DA} (see SI of (1)) for 5 seconds. Then the stimulus was delivered for 10
572 seconds, and the donor was excited every 0.5 seconds during this time. Before and after the donor
573 excitations, the acceptor was excited three times in 0.5-second intervals to measure I_{AA} (see SI of (1)).
574 After the stimulus was removed, the acceptor was excited three more times at 0.5-second intervals.
575 Imaging was then stopped and cells were allowed to adapt to the background for 120 seconds.

576 Stimulus protocols for measuring kinase linear response functions and fluctuations are described below.

577 At the end of each experiment, we delivered a long saturating stimulus (1 mM MeAsp plus 100 µM serine)
578 for 180 seconds to allow the cells to adapt. Then we removed the stimulus back to the background
579 concentration, eliciting a strong response from the cells, from which we determined the FRET signal at
580 maximum kinase activity. The donor was excited for 5 seconds before the saturating stimulus and 10
581 seconds after it, every 0.5 seconds. Before and after these donor excitations, the acceptor was excited
582 three times in 0.5-second intervals. The cells were exposed to the saturating stimulus for 180 seconds.
583 The donor was excited every 0.5 seconds for 5 seconds before cells were exposed to motility buffer with
584 Asp at background concentration c_0, followed by 10 seconds of additional donor excitations. Before and
585 after the donor excitations, the acceptor was again excited three times in 0.5-second intervals.

586 FRET signals were extracted as before (1). The FRET signal at minimum kinase activity, $FRET_{min}$, was
587 computed from the average FRET signal during the first saturating stimulus. The FRET signal at maximum
588 kinase activity, $FRET_{max}$, was computed from the average FRET signal during the first quarter (2.5
589 seconds) of the removal stimulus at the end of the experiment. Kinase activity was then computed from
590 corrected FRET signal: $a(t) = \frac{FRET(t) - FRET_{min}}{FRET_{max} - FRET_{min}}$.

591

592 Kinase linear response functions

593 Experiments were performed in Asp background concentrations c_0 of 0.1, 1, and 10 μM. Measurements
594 were made in single cells, and at least three replicates were performed per background. FRET level at
595 minimum kinase activity was measured at the beginning of each experiment, as described above. After
596 this, a series of stimuli were delivered to the cells in the microfluidic device. Cells were only illuminated
597 and imaged when stimulated in order to limit photobleaching. Before each stimulus, cells were imaged
598 for 7.5 seconds in the background concentration c_0. Then, the concentration of Asp was shifted up to
599 $c_+ > c_0$ for 30 seconds and imaging continued. Donor excitation interval was 0.75 seconds and acceptor
600 excitations were done before and after the set of donor excitations. After this, imaging was stopped and
601 the Asp concentration returned to c_0 for 65 seconds to allow cells to adapt. Then, the same process was
602 repeated, but this time shifting Asp concentration down to $c_- < c_0$. Alternating up and down stimuli were
603 repeated 10 times each. c_+ and c_- varied with each experiment and each background c_0. Finally, FRET
604 level at maximum kinase activity was measured at the end of each experiment, as described above. The
605 whole imaging protocol lasted <2200 seconds. In total, cells spent <60 minutes in the device, from loading
606 to the end of imaging.

607 These data were analyzed as before (1) to extract linear response parameters for each cell. In brief, the
608 responses of a cell to all steps up or steps down in concentration were averaged and the standard error
609 of the response at each time point computed. Model parameters were extracted by maximizing the
610 posterior probability of parameters given data, assuming a Gaussian likelihood function and log-uniform
611 priors for the parameters. The uncertainties of single-cell parameter estimates were generated by MCMC
612 sampling the posterior distribution. Finally, the population-median parameters were computed from all
613 cells in experiments in a given background c_0. Uncertainty $\sigma_{\theta_i}^2$ of the population-median value of
614 parameter θ_i, with $\theta = (G, \tau_1, \tau_2)$, was computed using:

615 $$\sigma_{\theta_i}^2 = \frac{1}{N}\left(1.4826\ \mathrm{mad}\left(\{\theta_i^{MAP}\}\right)\right)^2 + \frac{1}{N^2}\sum_k \left(\sigma_{\theta_i}^2\right)_k . \quad (18)$$

616 This expression accounts both for cell-to-cell variations (first term) and uncertainties in the single-cell
617 estimates (second term). N is the number of cells. $1.4826\ \mathrm{mad}(\ )$ is an outlier-robust uncertainty
618 estimate that coincides with the standard deviation when the samples are Gaussian-distributed, and
619 $\mathrm{mad}(\ )$ is the median absolute deviation, used previously (1). $\{\theta_i^{MAP}\}$ are the single-cell maximum *a-*
620 *posteriori* (MAP) estimates of parameter θ_i. $\left(\sigma_{\theta_i}^2\right)_k$ is the uncertainty of θ_i^{MAP} in cell k, which was
621 computed using

622 $$\left(\sigma_{\theta_i}\right)_k = 1.4826\ \mathrm{mad}\left(\left\{\hat{\theta}_i\right\}_k\right) \quad (19)$$

623 where $\left\{\hat{\theta}_i\right\}_k$ are the samples from the kth cell's posterior via Markov Chain Monte Carlo (MCMC).

624

625 <u>MWC kinase gain</u>

626 The estimated gain parameter G depended strongly on c_0, consistent with expectations from previous
627 work modeling kinase activity using the MWC model (e.g. (76)). In the MWC model, kinase-receptor
628 complexes can be in active or inactive states. The dissociation constants for the attractant in each state,
629 K_i and K_a, are different, with $K_i \ll K_a$, which causes attractant concentration to influence the fraction of

630 kinases in the active state. When the background concentration $c_0 \ll K_a$, the gain of the kinase response
631 to changes in log-concentration of attractant can be written:

632 $$G(c_0) = G_\infty \frac{c_0}{c_0 + K_i},$$

633 where G_∞ is the "log-sensing" gain (when $c_0 \gg K_i$). Parameters G_∞ and K_i were estimated by fitting the
634 estimates of G versus c_0. The fit was done by minimizing the sum of squared errors between the
635 logarithms of G and G_{MWC}. The estimated values of G vary by about an order of magnitude, and taking
636 the logarithms ensured that the smallest value of G had similar weight as largest value in the objective
637 function.

638

639 Statistics of noise in kinase activity

640 Fluctuations in kinase activity were measured in the same Asp background concentrations c_0 as above, as
641 well as $c_0 = 0$ μM. At least three replicate experiments were performed per background. FRET level at
642 minimum kinase activity was measured at the beginning of each experiment, as described above. After
643 these measurements, imaging was then stopped and cells were allowed to adapt to the background for
644 120 seconds. After this, cells were imaged for about 1200 seconds. Throughout, donor excitations were
645 done every 1.0 second, except when it was interrupted by acceptor excitations, which were conducted
646 every 100 donor excitations (see SI of (1)). Finally the FRET level at maximum kinase activity was measured
647 at the end of each experiment, as described above. The whole imaging protocol lasted <1400 seconds. In
648 total, cells spent about < 60 minutes in the device, from loading to the end of imaging.

649 These data were analyzed as before (1). Bayesian filtering methods (82) were used to compute the
650 likelihood of the parameters given the data, and the prior distribution was taken to be uniform in log.
651 Single-cell estimates and uncertainties of the noise parameters were extracted from the posterior
652 distribution as described above. In each background c_0, the population median parameter values were
653 computed, and their uncertainties were computed as described above, with $\theta = (D_n, \tau_n)$.

654

655 Swimming velocity statistics

656 Cells were prepared and imaged as before (1). After the second wash step of the Cell preparation section
657 above, cells were centrifuged again and resuspended in motility buffer containing a background
658 concentration of Asp c_0. The values of c_0 used here were the same as in the FRET experiments, including
659 $c_0 = 0$ μM. Then, the cell suspension was diluted to an OD600 of 0.00025. This low dilution of cells both
660 enables tracking and minimizes the effect of cells consuming Asp. The cell suspension was then loaded
661 into μ-Slide Chemotaxis devices (ibidi; Martinsried, Germany). Swimming cells were tracked in one of the
662 large reservoirs. 1000-s movies of swimming cells were recorded on a Nikon Ti-E Inverted Microscope
663 using a CFI Plan Fluor 4X objective (NA 0.13). Images were captured using a sCMOS camera (ORCA-Flash4.0
664 V2; Hamamatsu). Four biological replicates were performed for each background c_0.

665 Cell detection and tracking were carried out using the same custom MATLAB as we used previously (1),
666 with the same analysis parameters (see SI of that paper for details). Tumble detection was also carried
667 out identically as before (1). There was no minimum trajectory duration, but cells were kept only if at least

two tumbles were detected in their trajectory. For each cell, we computed the fraction of time spent in the "run" state P_{run}. Then we constructed the distribution of P_{run}, correcting for biases caused by the different diffusivities of cells with different P_{run} (1). As before (1), we then computed the correlation function of velocity along one spatial dimension for each cell, $V_i(t) = \langle v_x(t')v_x(t'+t)\rangle_{t'}$ among cells with P_{run} within ± 0.01 of the population-median value,. Finally, we computed a weighted average of the correlation functions over all cells in the population-median bin of P_{run}, where trajectories were weighted by their duration , giving $V(t)$. In each background c_0, for the median bin of P_{run}, the average trajectory duration was ~7.6 seconds, and the total trajectory time was $\geq 2.7 \times 10^4$ seconds.

These correlation functions $V(t)$ in each background c_0 and each experiment were fit to decaying exponentials $\sigma_v^2 \exp(-|t|/\tau_v)$, and the parameters and their uncertainties were extracted in two steps. First, we determined the MAP estimates of the parameters. An initial estimate of the parameters were esimated using the MATLAB *fit* function to fit exponentials to the $V(t)$ in the time rang $t \in [2\,\Delta t, 10\text{ s}]$, with $\Delta t = 50$ ms. The estimated τ_v was used to get the uncertainty of $V(t)$ in each experiment, as done before (1). Assuming a Gaussian likelihood function and parameters distributed uniformly in logarithm, the posterior distribution of parameter was constructed. In each experiment, MAP estimates of the parameters were extracted as done for the kinase parameters, and parameter uncertainties were computed from MCMC samples of the posterior distribution as above. Finally, we computed the average parameters σ_v^2 and τ_v over experimental replicates, as well as their standard errors over replicates.

Additional error analysis

Once the variance of the population-median value of parameter i was computed, $\sigma_{\theta_i}^2$, we propagated the uncertainty to functions of those parameters. For some function of the parameters, $f(\theta)$, we computed the variance of $f(\theta)$, σ_f^2, as:

$$\sigma_f^2 = \sum_i \left(\frac{\partial f}{\partial \theta_i}\right)^2 \sigma_{\theta_i}^2$$

$$= f^2 \sum_i \left(\frac{\partial \log f}{\partial \theta_i}\right)^2 \sigma_{\theta_i}^2. \tag{20}$$

The equations above neglect correlations in the uncertainties between pairs of parameters. This was used to compute the uncertainties of $\dot{I}_{s\to r}^*$, $\dot{I}_{s\to a}^*$, and η. The same formula was used to compute uncertainties of functions of time by applying the formula above pointwise at each time delay t and neglecting correlations in uncertainties between time points.

Acknowledgments: We thank … This work was supported by the Alfred P. Sloan Foundation under grant G-2023-19668 (HM, TE, BB); by NIH awards R01GM106189 (TE), R01GM138533 (TE), and R35GM138341 (BM); by Simons Investigator Award 624156 (BM); and by the JST PRESTO grant JPMJPR21E4 (KK); by the NSTC grant 112-2112-M-001-080-MY3. HM was supported by the Flatiron Institute, which is a division of the Simons Foundation. KK was also supported by the Institute of Molecular Biology, Academia Sinica.

Contributions: BM and HM conceived the project. KK, HM, TE, and BM designed the experiments. KK, JO, RK, and HM performed the experiments. HM and KK analyzed the data. HM and BM derived the theoretical results. HM wrote the first draft of the manuscript. HM, BM, KK, and TE edited the manuscript.

Competing interests: The authors declare no competing interests.

Data availability: Source data for the main text figures are provided online with the manuscript. Source data for the Supplementary Figures are contained in a Supplementary Data file.

Code availability: Code to reproduce the main text figures are available with the source data. All algorithms used are described in detail in the Supplementary Information.

716 **References**

717 1. Mattingly HH, Kamino K, Machta BB, Emonet T. Escherichia coli chemotaxis is information limited.
718 Nat Phys. 2021 Dec;17(12):1426–31.

719 2. Berg HC, Purcell EM. Physics of chemoreception. Biophysical Journal. 1977 Nov 1;20(2):193–219.

720 3. Osborne LC, Lisberger SG, Bialek W. A sensory source for motor variation. Nature. 2005
721 Sep;437(7057):412–6.

722 4. Hecht S, Shlaer S, Pirenne MH. ENERGY, QUANTA, AND VISION. Journal of General Physiology. 1942
723 Jul 20;25(6):819–40.

724 5. Barlow HB. The Size of Ommatidia in Apposition Eyes. Journal of Experimental Biology. 1952 Dec
725 1;29(4):667–74.

726 6. Rieke F, Baylor DA. Single-photon detection by rod cells of the retina. Rev Mod Phys. 1998 Jul
727 1;70(3):1027–36.

728 7. Bialek W. Biophysics: Searching for Principles [Internet]. Princeton University Press; 2012 [cited
729 2020 Jun 18]. Available from:
730 https://press.princeton.edu/books/hardcover/9780691138916/biophysics

731 8. Brumley DR, Carrara F, Hein AM, Yawata Y, Levin SA, Stocker R. Bacteria push the limits of
732 chemotactic precision to navigate dynamic chemical gradients. PNAS. 2019 May 28;116(22):10792–
733 7.

734 9. Sinha SR, Bialek W, van Steveninck RR de R. Optimal Local Estimates of Visual Motion in a Natural
735 Environment. Phys Rev Lett. 2021 Jan 4;126(1):018101.

736 10. Govern CC, Wolde PR ten. Optimal resource allocation in cellular sensing systems. PNAS. 2014 Dec
737 9;111(49):17486–91.

738 11. Malaguti G, ten Wolde PR. Theory for the optimal detection of time-varying signals in cellular
739 sensing systems. Goldstein RE, Weigel D, editors. eLife. 2021 Feb 17;10:e62574.

740 12. Tjalma AJ, Galstyan V, Goedhart J, Slim L, Becker NB, ten Wolde PR. Trade-offs between cost and
741 information in cellular prediction. Proceedings of the National Academy of Sciences. 2023 Oct
742 10;120(41):e2303078120.

743 13. Tjalma AJ, Wolde PR ten. Predicting concentration changes via discrete sampling [Internet]. arXiv;
744 2024 [cited 2024 Feb 15]. Available from: http://arxiv.org/abs/2402.05825

745 14. Lan G, Sartori P, Neumann S, Sourjik V, Tu Y. The energy–speed–accuracy trade-off in sensory
746 adaptation. Nature Physics. 2012 May;8(5):422–8.

747 15. Cao Y, Wang H, Ouyang Q, Tu Y. The free-energy cost of accurate biochemical oscillations. Nature
748 Phys. 2015 Sep;11(9):772–8.

749 16. Zhang D, Cao Y, Ouyang Q, Tu Y. The energy cost and optimal design for synchronization of coupled
750 molecular oscillators. Nat Phys. 2020 Jan;16(1):95–100.

751 17. Bryant SJ, Machta BB. Physical Constraints in Intracellular Signaling: The Cost of Sending a Bit. Phys
752 Rev Lett. 2023 Aug 7;131(6):068401.

753 18. Clark DA, Grant LC. The bacterial chemotactic response reflects a compromise between transient
754 and steady-state behavior. PNAS. 2005 Jun 28;102(26):9150–5.

755 19. Celani A, Vergassola M. Bacterial strategies for chemotaxis response. PNAS. 2010 Jan
756 26;107(4):1391–6.

757 20. Cremer J, Honda T, Tang Y, Wong-Ng J, Vergassola M, Hwa T. Chemotaxis as a navigation strategy to
758 boost range expansion. Nature. 2019 Nov;575(7784):658–63.

759 21. Ni B, Colin R, Link H, Endres RG, Sourjik V. Growth-rate dependent resource investment in bacterial
760 motile behavior quantitatively follows potential benefit of chemotaxis. PNAS. 2020 Jan
761 7;117(1):595–601.

762 22. Shimizu TS, Tu Y, Berg HC. A modular gradient-sensing network for chemotaxis in Escherichia coli
763 revealed by responses to time-varying stimuli. Molecular Systems Biology. 2010 Jan 1;6(1):382.

764 23. Tu Y. Quantitative Modeling of Bacterial Chemotaxis: Signal Amplification and Accurate Adaptation.
765 Annual Review of Biophysics. 2013;42(1):337–59.

766 24. Parkinson JS, Hazelbauer GL, Falke JJ. Signaling and sensory adaptation in Escherichia coli
767 chemoreceptors: 2015 update. Trends in Microbiology. 2015 May 1;23(5):257–66.

768 25. Berg HC. E. coli in motion. New York: Springer; 2004. 133 p. (Biological and medical physics series).

769 26. Bialek W, Setayeshgar S. Physical limits to biochemical signaling. PNAS. 2005 Jul 19;102(29):10040–
770 5.

771 27. Kaizu K, de Ronde W, Paijmans J, Takahashi K, Tostevin F, ten Wolde PR. The Berg-Purcell Limit
772 Revisited. Biophysical Journal. 2014 Feb 18;106(4):976–85.

773 28. ten Wolde PR, Becker NB, Ouldridge TE, Mugler A. Fundamental Limits to Cellular Sensing. J Stat
774 Phys. 2016 Mar 1;162(5):1395–424.

775 29. Endres RG, Wingreen NS. Maximum Likelihood and the Single Receptor. Phys Rev Lett. 2009 Oct
776 7;103(15):158101.

777 30. Mehta P, Schwab DJ. Energetic costs of cellular computation. PNAS. 2012 Oct 30;109(44):17978–82.

778 31. Lang AH, Fisher CK, Mora T, Mehta P. Thermodynamics of Statistical Inference by Cells. Phys Rev
779 Lett. 2014 Oct 3;113(14):148103.

780 32. Govern CC, ten Wolde PR. Energy Dissipation and Noise Correlations in Biochemical Sensing. Phys
781 Rev Lett. 2014 Dec 16;113(25):258102.

33. Mora T, Nemenman I. Physical Limit to Concentration Sensing in a Changing Environment. Phys Rev Lett. 2019 Nov 5;123(19):198101.

34. Malaguti G, ten Wolde PR. Receptor time integration via discrete sampling. Phys Rev E. 2022 May 11;105(5):054406.

35. Mora T, Wingreen NS. Limits of Sensing Temporal Concentration Changes by Single Cells. Phys Rev Lett. 2010 Jun 14;104(24):248101.

36. Hein AM, Brumley DR, Carrara F, Stocker R, Levin SA. Physical limits on bacterial navigation in dynamic environments. Journal of The Royal Society Interface. 2016 Jan 31;13(114):20150844.

37. Aquino G, Wingreen NS, Endres RG. Know the Single-Receptor Sensing Limit? Think Again. J Stat Phys. 2016 Mar 1;162(5):1353–64.

38. Cover TM, Thomas JA. Elements of Information Theory. New York, NY: Wiley-Interscience; 1991.

39. Sigtermans D. Towards a Framework for Observational Causality from Time Series: When Shannon Meets Turing. Entropy. 2020 Apr;22(4):426.

40. Schreiber T. Measuring Information Transfer. Phys Rev Lett. 2000 Jul 10;85(2):461–4.

41. Shannon CE. A Mathematical Theory of Communication. Bell System Technical Journal. 1948;27(3):379–423.

42. Bialek W, Nemenman I, Tishby N. Predictability, complexity, and learning. Neural Comput. 2001 Nov;13(11):2409–63.

43. Bialek W, De Ruyter Van Steveninck RR, Tishby N. Efficient representation as a design principle for neural coding and computation. In: 2006 IEEE International Symposium on Information Theory. 2006. p. 659–63.

44. Becker NB, Mugler A, ten Wolde PR. Optimal Prediction by Cellular Signaling Networks. Phys Rev Lett. 2015 Dec 17;115(25):258103.

45. Palmer SE, Marre O, Berry MJ, Bialek W. Predictive information in a sensory population. PNAS. 2015 Jun 2;112(22):6908–13.

46. Sachdeva V, Mora T, Walczak AM, Palmer SE. Optimal prediction with resource constraints using the information bottleneck. PLOS Computational Biology. 2021 Mar 8;17(3):e1008743.

47. Wang S, Segev I, Borst A, Palmer S. Maximally efficient prediction in the early fly visual system may support evasive flight maneuvers. PLOS Computational Biology. 2021 May 20;17(5):e1008965.

48. Tjalma AJ, Galstyan V, Goedhart J, Slim L, Becker NB, Wolde PR ten. Trade-offs between cost and information in cellular prediction [Internet]. bioRxiv; 2023 [cited 2023 Jan 12]. p. 2023.01.10.523390. Available from: https://www.biorxiv.org/content/10.1101/2023.01.10.523390v1

815 49. Lovely PS, Dahlquist FW. Statistical measures of bacterial motility and chemotaxis. Journal of
816 Theoretical Biology. 1975 Apr 1;50(2):477–96.

817 50. Kolmogorov AN. Interpolation and Extrapolation of Stationary Sequences. Izvestiya the Academy of
818 Sciences of the USSR. 1941;5:3–14.

819 51. Kolmogorov AN. Stationary sequences in Hilbert space. Bull Moscow Univ. 1941;2(6):1–40.

820 52. Wiener N. Extrapolation, Interpolation, and Smoothing of Stationary Time Series: With Engineering
821 Applications. Cambridge, MA, USA: MIT Press; 1949. 163 p.

822 53. Andrews BW, Yi TM, Iglesias PA. Optimal Noise Filtering in the Chemotactic Response of Escherichia
823 coli. PLOS Computational Biology. 2006 Nov 17;2(11):e154.

824 54. Hinczewski M, Thirumalai D. Cellular Signaling Networks Function as Generalized Wiener-
825 Kolmogorov Filters to Suppress Noise. Phys Rev X. 2014 Oct 29;4(4):041017.

826 55. Husain K, Pittayakanchit W, Pattanayak G, Rust MJ, Murugan A. Kalman-like Self-Tuned Sensitivity in
827 Biophysical Sensing. Cell Systems. 2019 Nov;9(5):459-465.e6.

828 56. Segall JE, Block SM, Berg HC. Temporal comparisons in bacterial chemotaxis. PNAS. 1986 Dec
829 1;83(23):8987–91.

830 57. Korobkova E, Emonet T, Vilar JMG, Shimizu TS, Cluzel P. From molecular noise to behavioural
831 variability in a single bacterium. Nature. 2004 Apr;428(6982):574–8.

832 58. Colin R, Rosazza C, Vaknin A, Sourjik V. Multiple sources of slow activity fluctuations in a bacterial
833 chemosensory network. Barkai N, editor. eLife. 2017 Dec 12;6:e26796.

834 59. Keegstra JM, Kamino K, Anquez F, Lazova MD, Emonet T, Shimizu TS. Phenotypic diversity and
835 temporal variability in a bacterial signaling network revealed by single-cell FRET. Barkai N, editor.
836 eLife. 2017 Dec 12;6:e27455.

837 60. Francis NR, Levit MN, Shaikh TR, Melanson LA, Stock JB, DeRosier DJ. Subunit Organization in a
838 Soluble Complex of Tar, CheW, and CheA by Electron Microscopy. J Biol Chem. 2002 Sep
839 27;277(39):36755–9.

840 61. Levit MN, Grebe TW, Stock JB. Organization of the Receptor-Kinase Signaling Array That Regulates
841 Escherichia coli Chemotaxis. J Biol Chem. 2002 Sep 27;277(39):36748–54.

842 62. Yang Y, M. Pollard A, Höfler C, Poschet G, Wirtz M, Hell R, et al. Relation between chemotaxis and
843 consumption of amino acids in bacteria. Molecular Microbiology. 2015;96(6):1272–82.

844 63. Spudich JL, Koshland DE. Non-genetic individuality: chance in the single cell. Nature. 1976
845 Aug;262(5568):467–71.

846 64. Park H, Pontius W, Guet CC, Marko JF, Emonet T, Cluzel P. Interdependence of behavioural
847 variability and response to small stimuli in bacteria. Nature. 2010 Dec;468(7325):819–23.

848 65. Park H, Oikonomou P, Guet CC, Cluzel P. Noise Underlies Switching Behavior of the Bacterial
849 Flagellum. Biophysical Journal. 2011 Nov 16;101(10):2336–40.

850 66. Masson JB, Voisinne G, Wong-Ng J, Celani A, Vergassola M. Noninvasive inference of the molecular
851 chemotactic response using bacterial trajectories. PNAS. 2012 Jan 31;109(5):1802–7.

852 67. Dufour YS, Gillet S, Frankel NW, Weibel DB, Emonet T. Direct Correlation between Motile Behavior
853 and Protein Abundance in Single Cells. PLOS Computational Biology. 2016 Sep 6;12(9):e1005041.

854 68. Waite AJ, Frankel NW, Dufour YS, Johnston JF, Long J, Emonet T. Non-genetic diversity modulates
855 population performance. Molecular Systems Biology. 2016 Dec 1;12(12):895.

856 69. Fu X, Kato S, Long J, Mattingly HH, He C, Vural DC, et al. Spatial self-organization resolves conflicts
857 between individuality and collective migration. Nature Communications. 2018 Jun 5;9(1):2177.

858 70. Kamino K, Keegstra JM, Long J, Emonet T, Shimizu TS. Adaptive tuning of cell sensory diversity
859 without changes in gene expression. Science Advances. 2020;

860 71. Kamino K, Kadakia N, Aoki K, Shimizu TS, Emonet T. Optimal inference of molecular interactions in
861 live FRET imaging [Internet]. bioRxiv; 2022 [cited 2022 Aug 20]. p. 2022.03.29.486267. Available
862 from: https://www.biorxiv.org/content/10.1101/2022.03.29.486267v1

863 72. Moore JP, Kamino K, Kottou R, Shimizu TS, Emonet T. Signal integration and adaptive sensory
864 diversity tuning in Escherichia coli chemotaxis. Cell Systems. 2024;15.

865 73. Sourjik V, Berg HC. Receptor sensitivity in bacterial chemotaxis. Proceedings of the National
866 Academy of Sciences. 2002 Jan 8;99(1):123–7.

867 74. Sourjik V, Berg HC. Functional interactions between receptors in bacterial chemotaxis. Nature. 2004
868 Mar;428(6981):437–41.

869 75. Monod J, Wyman J, Changeux JP. On the nature of allosteric transitions: A plausible model. Journal
870 of Molecular Biology. 1965 May 1;12(1):88–118.

871 76. Mello BA, Tu Y. An allosteric model for heterogeneous receptor complexes: Understanding bacterial
872 chemotaxis responses to multiple stimuli. PNAS. 2005 Nov 29;102(48):17354–9.

873 77. Keymer JE, Endres RG, Skoge M, Meir Y, Wingreen NS. Chemosensing in Escherichia coli: Two
874 regimes of two-state receptors. PNAS. 2006 Feb 7;103(6):1786–91.

875 78. Moore JP, Kamino K, Emonet T. Non-Genetic Diversity in Chemosensing and Chemotactic Behavior.
876 International Journal of Molecular Sciences. 2021 Jan;22(13):6960.

877 79. Kalinin YV, Jiang L, Tu Y, Wu M. Logarithmic Sensing in Escherichia coli Bacterial Chemotaxis.
878 Biophysical Journal. 2009 Mar 18;96(6):2439–48.

879 80. Lazova MD, Ahmed T, Bellomo D, Stocker R, Shimizu TS. Response rescaling in bacterial chemotaxis.
880 PNAS. 2011 Aug 16;108(33):13870–5.

881 81. Adler M, Alon U. Fold-change detection in biological systems. Current Opinion in Systems Biology.
882 2018 Apr 1;8:81–9.

883 82. Sarkka S. Bayesian Filtering and Smoothing [Internet]. Cambridge: Cambridge University Press; 2013
884 [cited 2020 Jun 30]. Available from: http://ebooks.cambridge.org/ref/id/CBO9781139344203

885 83. Khursigara CM, Lan G, Neumann S, Wu X, Ravindran S, Borgnia MJ, et al. Lateral density of receptor
886 arrays in the membrane plane influences sensitivity of the E. coli chemotaxis response. EMBO J.
887 2011 May 4;30(9):1719–29.

888 84. Hazel JR, Sidell BD. A method for the determination of diffusion coefficients for small molecules in
889 aqueous solution. Analytical Biochemistry. 1987 Nov 1;166(2):335–41.

890 85. Cremer J, Segota I, Yang C yu, Arnoldini M, Sauls JT, Zhang Z, et al. Effect of flow and peristaltic
891 mixing on bacterial growth in a gut-like channel. PNAS. 2016 Oct 11;113(41):11414–9.

892 86. Sartori P, Tu Y. Free Energy Cost of Reducing Noise while Maintaining a High Sensitivity. Phys Rev
893 Lett. 2015 Sep 8;115(11):118102.

894 87. Mehta P, Lang AH, Schwab DJ. Landauer in the age of synthetic biology: energy consumption and
895 information processing in biochemical networks. J Stat Phys. 2016 Mar;162(5):1153–66.

896 88. Hathcock D, Yu Q, Mello BA, Amin DN, Hazelbauer GL, Tu Y. A nonequilibrium allosteric model for
897 receptor-kinase complexes: The role of energy dissipation in chemotaxis signaling. Proceedings of
898 the National Academy of Sciences. 2023 Oct 17;120(42):e2303115120.

899 89. Hathcock D, Yu Q, Tu Y. Time-reversal symmetry breaking in the chemosensory array: asymmetric
900 switching and dissipation-enhanced sensing [Internet]. arXiv; 2023 [cited 2024 Jan 10]. Available
901 from: http://arxiv.org/abs/2312.17424

902 90. Sherry DM, Graf IR, Bryant SJ, Emonet T, Machta BB. Lattice ultrasensitivity produces large gain in E.
903 coli chemosensing [Internet]. bioRxiv; 2024 [cited 2024 Jun 14]. p. 2024.05.28.596300. Available
904 from: https://www.biorxiv.org/content/10.1101/2024.05.28.596300v1

905 91. Adler J. Chemotaxis in Bacteria. Science. 1966 Aug 12;153(3737):708–16.

906 92. de Gennes PG. Chemotaxis: the role of internal delays. Eur Biophys J. 2004 Dec 1;33(8):691–3.

907 93. Wong-Ng J, Melbinger A, Celani A, Vergassola M. The Role of Adaptation in Bacterial Speed Races.
908 PLOS Computational Biology. 2016 Jun 3;12(6):e1004974.

909 94. Phan TV, Mattingly HH, Vo L, Marvin JS, Looger LL, Emonet T. Direct measurement of dynamic
910 attractant gradients reveals breakdown of the Patlak–Keller–Segel chemotaxis model. Proceedings
911 of the National Academy of Sciences. 2024 Jan 16;121(3):e2309251121.

912 95. Narla AV, Cremer J, Hwa T. A traveling-wave solution for bacterial chemotaxis with growth.
913 Proceedings of the National Academy of Sciences. 2021 Nov 30;118(48):e2105138118.

914 96. Mattingly HH, Emonet T. Collective behavior and nongenetic inheritance allow bacterial populations
915 to adapt to changing environments. Proceedings of the National Academy of Sciences. 2022 Jun
916 28;119(26):e2117377119.

917 97. Armstrong JB, Adler J, Dahl MM. Nonchemotactic Mutants of Escherichia coli. Journal of
918 Bacteriology. 1967;93(1):390–8.

919 98. Bachmann BJ. Pedigrees of Some Mutant Strains of Escherichia coli K-12. 1972;36:33.

920 99. Barker CS, Prüß BM, Matsumura P. Increased Motility of Escherichia coli by Insertion Sequence
921 Element Integration into the Regulatory Region of the flhD Operon. Journal of Bacteriology. 2004
922 Nov 15;186(22):7529–37.

923 100. Briegel A, Ortega DR, Tocheva EI, Wuichet K, Li Z, Chen S, et al. Universal architecture of
924 bacterial chemoreceptor arrays. Proceedings of the National Academy of Sciences. 2009 Oct
925 6;106(40):17181–6.

926 101. Waite AJ, Frankel NW, Emonet T. Behavioral Variability and Phenotypic Diversity in Bacterial
927 Chemotaxis. Annual Review of Biophysics. 2018;47(1):595–616.

928 102. Li L, Zhang X, Sun Y, Ouyang Q, Tu Y, Luo C. Phenotypic Variability Shapes Bacterial Responses to
929 Opposing Gradients. PRX Life. 2024 Jan 9;2(1):013001.

930 103. Qin D, Xia Y, Whitesides GM. Soft lithography for micro- and nanoscale patterning. Nature
931 Protocols. 2010 Mar;5(3):491–502.

932 104. Edelstein A, Amodaj N, Hoover K, Vale R, Stuurman N. Computer Control of Microscopes Using
933 µManager. Current Protocols in Molecular Biology. 2010;92(1):14.20.1-14.20.17.

934 105. Zal T, Gascoigne NRJ. Photobleaching-Corrected FRET Efficiency Imaging of Live Cells. Biophysical
935 Journal. 2004 Jun 1;86(6):3923–39.

936